J. Fluid Mech. (1989), *vol.* 198, *pp.* 127–153
Printed in Great Britain

On the first-mode instability in subsonic, supersonic or hypersonic boundary layers

By F. T. SMITH
Mathematics Department, University College, Gower Street, London, WC1E 6BT, UK

(Received 20 October 1987)

The work, addressing subsonic, supersonic and hypersonic boundary-layer instability, is motivated by the need for more understanding of compressible transition at high global Reynolds numbers Re. In the supersonic case, the so-called 'first modes' of instability found/suggested by previous Orr–Sommerfeld computations can be identified as triple-deck oblique ones, directed outside the local wave-Mach-cone directions. Less oblique instability modes inside are not of Orr–Sommerfeld form since they are substantially affected by non-parallel flow effects. The maximum linear growth rates are determined for a range of supersonic and subsonic free-stream Mach numbers M_∞, and comparisons are made with previous computations, showing fairly good agreement at moderate Mach numbers. A second mound of unstable wavenumbers and frequencies is also evident. In addition, the nonlinear version is set up and emphasized (with attention drawn to a recent paper by the author (1988*a*) showing the possibility of nonlinear break-up), and certain extremes are examined including those of transonic and hypersonic boundary layers. In the hypersonic limit a new regime is found (for many conditions, including the insulated plate), namely $M_\infty \sim Re^{\frac{1}{10}}$, in which non-parallel-flow effects enter to control the main disturbances, and it is concluded that the restriction $M_\infty \ll Re^{\frac{1}{10}}$ applies to the Orr–Sommerfeld approach. This is a very severe restriction in practice.

1. Introduction

There is much renewed technological and scientific interest currently in supersonic and hypersonic flows, in addition to the subsonic regime, and in compressible boundary-layer instability and transition in particular. Although relatively few experimental results on supersonic boundary-layer transition are available (see Laufer & Vrebalovich 1960; Pate & Schueler 1969; Kendall 1975; Lysenko & Maslov 1984), a fairly large body of interesting computational results exists due to Mack (1975, 1984, 1986 and references therein), principally, and Malik (1982, 1987) and others, concerning the linear viscous and inviscid instability of two-dimensional compressible boundary layers at various Mach numbers. A major finding from these computations at large Reynolds numbers is that, typically, as the Mach number is increased, the instability features are dominated by the so-called 'first mode' up to a Mach number of about 4 and by the 'second mode' thereafter, with the first modes having their maximum growth rates for oblique three-dimensional waves and being described as viscous, whereas the second modes are mainly inviscid and the maximum growth rates are for the two-dimensional waves.

The reasons for the current investigation of subsonic, supersonic and hypersonic boundary-layer instability are four-fold. First we present an alternative approach for the first-mode response based on assuming that the characteristic global Reynolds

number (Re) is a large parameter. This has the double advantage of turning the parallel-flow approximation for the basic flow into a rational step, as opposed to the convenient but rather suspect irrational step it represents (strictly) in the previous Orr–Sommerfeld-type computations, and of providing an asymptotic framework, understanding and results with which the previous computations can be compared: see later. Second, the soundness of the Orr–Sommerfeld approach with regard to the neglect of non-parallel-flow effects is re-examined, leading to the (severe) limitation (1.2) below. Third, the work shows that the first modes described above are in fact of the viscous–inviscid interactive kind and are governed generally by the subsonic or supersonic triple-deck structure extended to three-dimensional unsteady motions, just as for the incompressible Tollmien–Schlichting case (e.g. Smith 1979*a*, *b*; Smith & Stewart 1987; see also Smith 1988*a*) in effect, except that in the supersonic case these first modes of instability must be three-dimensional and be directed outside of the local wave-Mach-cone directions, i.e. at wave angles θ satisfying

$$\theta > \tan^{-1}\{(M_\infty^2 - 1)^{\frac{1}{2}}\}, \tag{1.1}$$

where M_∞ is the local Mach number of the external stream. Any unstable three- and two-dimensional supersonic waves that are less obliquely inclined are found to suffer from strong non-parallel-flow effects (see §5) because their lengthscales are much greater, comparable with the development length of the basic compressible boundary layer. Fourth, the present approach opens the way readily to the study of the nonlinear responses which are vital to subsonic, supersonic or hypersonic transition. Such responses can be catered for in the nonlinear three-dimensional unsteady triple-deck equations, or in their finite-Re counterpart, the interacting boundary-layer equations.

In more detail, §2 below gives, for supersonic flow, the scales involved for the first modes and the governing equations, which are cast in the nonlinear triple-deck mould first, for three-dimensional unsteady motion, with the linearized version then providing the required large-Re asymptote for the Orr–Sommerfeld problem, subject to the condition in (1.1). Section 3 then presents the numerical results and compares these with the previous computations. The agreement turns out to be reasonably encouraging, qualitatively and quantitatively, bearing in mind the asymptotic nature of the theory on the one hand and, on the other, the violation of the restrictions (1.1) and (1.2) below by the previous Orr–Sommerfeld computations, among other things. We devote §4 to a study of the various extremes of interest, one being for a second mound of instability which is seen to emerge during the calculations of §3, a mound that seems to have received scant attention previously and is different from the second modes mentioned above. Another extreme of much practical and theoretical concern is the hypersonic limit where M_∞ becomes large, and there the first modes' main wavelengths elongate considerably, forcing non-parallel-flow effects to enter play at leading order when M_∞ becomes as large as $Re^{\frac{1}{10}}$ (in many cases, including that of an insulated wall: see §5). Thus the validity of the parallel-flow approximation, which is at the heart of the Orr–Sommerfeld approach for example, is restricted to $M_\infty \ll Re^{\frac{1}{10}}$ or, in terms of the local Reynolds number R_δ based on the boundary-layer thickness and $R \equiv Re^{\frac{1}{2}}$, the restriction is

$$M_\infty \ll R_\delta^{\frac{1}{5}}, \quad \text{i.e. } M_\infty \ll R^{\frac{1}{5}}. \tag{1.2}$$

This extra limitation found on the use of the Orr–Sommerfeld approach for first modes is a very severe one in practice. For a typical R of 1500, for instance, (1.2) formally restricts the Mach-number range to $M_\infty \ll 4.3$, thereby casting doubt on the numerous previous computations at higher Mach numbers up to 10 and beyond.

Other extremes addressed in §4 concern transonic flow, high frequencies, and the cut-off implied by (1.1). All these extremes add analytical support to the numerical work of §3. Further discussion, including the subsonic version, is presented in §5.

Regarding notation, we use the velocity components u, v, w, the corresponding Cartesian coordinates x, y, z, the pressure p, the density ρ and the time t non-dimensionalized with respect to the free-stream speed u_∞^*, the typical streamwise length $l^*, \rho_\infty^* u_\infty^{*2}$, the free-stream density ρ_∞^* and l^*/u_∞^*. The subscripts ∞, w stand for the free-stream and plate values respectively. Here the boundary layer is taken to be the two-dimensional steady one on an aligned flat plate $y = 0, x > 0$, with characteristic scales $x \sim 1$, $y \sim Re^{-\frac{1}{2}}$ at general $O(1)$ free-stream Mach numbers M_∞, where the Reynolds number $Re \equiv u_\infty^* l^*/\nu_\infty^*$ is large. The boundary-layer profiles of the temperature T^*, of ρ ($= R_0$ say), of u ($= U_0$ say), and of Mach number, are smooth (e.g. see Stewartson 1964) with T^* varying from the plate temperature T_w^* to the external temperature T_∞^*, the ratio T_w^*/T_∞^* is generally $O(1)$, and the Chapman viscosity law is assumed for definiteness, so that $\mu^*/T^* = C\mu_\infty^*/T_\infty^*$ ($= \mu_w^*/T_w^*$), where C is constant and μ^* is the viscosity $\rho^* \nu^*$ (see e.g. Stewartson 1964). It should be emphasized that virtually all the above assumptions can be relaxed to cater for the more general boundary layer, however, since only the local external and plate conditions substantially affect the present instabilities at any chosen station $(x, z) = (x_0, z_0)$ with x_0 of $O(1)$ [subsequently we take $x_0 = 1$, this essentially fixing l^* and Re]. In particular, the plate may be insulated or at prescribed temperature; see also a note in §2 with regard to the energy equation. Also, $\lambda \approx 0.332 x_0^{-\frac{1}{2}}$ is the local skin-friction factor, ϵ is used to denote $Re^{-\frac{1}{8}}$ for convenience, and the subscripts r, i stand for the real and imaginary parts respectively, while c.c. stands for the complex conjugate.

2. Scales and governing equations

The first modes in supersonic boundary-layer instability are three-dimensional, of the viscous–inviscid Tollmien–Schlichting (TS) kind, we argue, and they take on the triple-deck form at large Reynolds numbers Re along and near the lower branch that is of interest here. Thus their normal y-variation exhibits three main scales, with $y \sim \epsilon^5 (M_\infty^2 - 1)^{-\frac{1}{8}} (T_w^*/T_\infty^*)^{\frac{3}{2}}$ in the lower deck which is the viscous sublayer containing the critical layer effectively, $y \sim \epsilon^4 (T_w^*/T_\infty^*)$ in the main deck comprising most of the boundary layer, and $y \sim \epsilon^3 (M_\infty^2 - 1)^{-\frac{7}{8}} (T_w^*/T_\infty^*)^{\frac{3}{2}}$ in the upper deck of potential flow just outside the boundary layer. The expansions of the flow solution in the decks can be picked out from previous work on supersonic triple-deck interactions (e.g. Stewartson & Williams 1969; Stewartson 1974), but extended to three-dimensional unsteady motion, and as a reminder we summarize the expansions and scalings below, noting that the procedure used first sets up the more general *nonlinear* unsteady interaction, from which the *linear* instability problem is readily deduced. An alternative procedure is to obtain the linear problem directly from the linearized Navier–Stokes equations or from the Orr–Sommerfeld approximation, although the latter is not strictly rational at finite Re values. Both procedures have been followed in previous incompressible-instability studies (Smith 1979*a*, *b*, 1985, 1986; Smith & Stewart 1987 and see §5 below for the subsonic counterpart), incidentally, but the nonlinear approach has the obvious advantage of initially posing, and emphasizing, a problem more relevant to transition ultimately (e.g. see the nonlinear break-up process described by Smith 1988*a*) than is linear instability theory.

The first-mode lengthscale (L_x, say) is $O(Re^{-\frac{3}{8}})$, long compared with the boundary-

layer thickness but short relative to the $O(1)$ development length of the boundary layer, and the timescale is also fast relative to the maximum convective scale, specifically

$$[x-x_0, z-z_0] = \epsilon^3 K_1[X, Z], \quad K_1 \equiv \frac{C^{\frac{3}{8}}(T_w^*/T_\infty^*)^{\frac{3}{2}}}{\lambda^{\frac{5}{4}}(M_\infty^2-1)^{\frac{3}{8}}}, \tag{2.1a–c}$$

$$t = \epsilon^2(M_\infty^2-1)^{-\frac{1}{4}}(T_w^*/T_\infty^*)\, C^{\frac{1}{4}}\lambda^{-\frac{3}{2}}\hat{t}. \tag{2.1d}$$

In the viscous sublayer, or lower deck, $y = \epsilon^5(M_\infty^2-1)^{-\frac{1}{8}}C^{\frac{5}{8}}(T_w^*/T_\infty^*)^{\frac{3}{2}}\lambda^{-\frac{3}{4}}Y$ and to leading order

$$u = \epsilon C^{\frac{1}{8}}(T_w^*/T_\infty^*)^{\frac{1}{2}}\lambda^{\frac{1}{4}}(M_\infty^2-1)^{-\frac{1}{8}}U, \tag{2.2a}$$

$$v = \epsilon^3 C^{\frac{3}{8}}(T_w^*/T_\infty^*)^{\frac{1}{2}}\lambda^{\frac{3}{4}}(M_\infty^2-1)^{\frac{1}{8}}V, \tag{2.2b}$$

$$w = \epsilon C^{\frac{1}{8}}(T_w^*/T_\infty^*)^{\frac{1}{2}}\lambda^{\frac{1}{4}}(M_\infty^2-1)^{-\frac{1}{8}}W, \tag{2.2c}$$

$$p-p_\infty = \epsilon^2 C^{\frac{1}{4}}\lambda^{\frac{1}{2}}(M_\infty^2-1)^{-\frac{1}{4}}P. \tag{2.2d}$$

Here and below the factors involving $C, \lambda, M_\infty, T_w^*/T_\infty^*$ are introduced to normalize the resultant governing equations, which from the Navier–Stokes equations are

$$U_X + V_Y + W_Z = 0, \tag{2.3a}$$

$$U_{\hat{t}} + UU_X + VU_Y + WU_Z = -P_X(X, Z, \hat{t}) + U_{YY}, \tag{2.3b}$$

$$W_{\hat{t}} + UW_X + VW_Y + WW_Z = -P_Z(X, Z, \hat{t}) + W_{YY}, \tag{2.3c}$$

in the lower deck, with the y-momentum equation yielding the result that $\partial P/\partial Y = 0$. A reminder concerning the energy equation should be noted, namely that its influence is of higher order, as Stewartson & Williams (1969) show, since the temperature and density are effectively uniform (and generally $O(1)$ in non-dimensional terms) across the lower deck as this deck forms only a small fraction of the original boundary layer. The principal boundary conditions here are

$$U = V = W = 0 \quad \text{at} \quad Y = 0, \tag{2.3d}$$

$$U \sim Y + A(X, Z, \hat{t}), \quad W \to 0 \quad \text{as} \quad Y \to \infty, \tag{2.3e}$$

for no slip at the solid surface and for matching with the main deck, $-A$ representing the unknown relative displacement. Next, the main deck has $y = \epsilon^4 C^{\frac{1}{2}}(T_w^*/T_\infty^*)\,\tilde{y}$ and merely transmits the small displacement effect across the boundary layer as well as smoothing out the induced velocity component w, in the form

$$u = U_0(\tilde{y}) + \epsilon C^{\frac{1}{8}}(T_w^*/T_\infty^*)^{\frac{1}{2}}(M_\infty^2-1)^{-\frac{1}{8}}\lambda^{-\frac{3}{4}}AU_0'(\tilde{y}) + \ldots, \tag{2.4a}$$

$$v = -\epsilon^2 C^{\frac{1}{4}}\lambda^{\frac{1}{2}}(M_\infty^2-1)^{\frac{1}{4}}A_X\, U_0(\tilde{y}) + \ldots, \tag{2.4b}$$

$$w = \epsilon^2 C^{\frac{1}{4}}\lambda^{\frac{1}{2}}(M_\infty^2-1)^{-\frac{1}{4}}(T_w^*/T_\infty^*)\, DR_0(0)/R_0(\tilde{y})\, U_0(\tilde{y}) + \ldots, \tag{2.4c}$$

$$p-p_\infty = \epsilon^2 C^{\frac{1}{4}}\lambda^{\frac{1}{2}}(M_\infty^2-1)^{-\frac{1}{4}}P(X, Z, \hat{t}) + \ldots, \tag{2.4d}$$

with a similar small displacement occurring in the density and temperature profiles. Here the unknown function $D(X, Z, \hat{t})$ satisfies $D_X = -P_Z$ from the spanwise momentum balance and (2.4c) shows the jet-like response in the cross-flow due to the spanwise variation in the pressure, the velocity w reaching its maximum amplitude inside the lower deck. The third, upper, deck then occurs where $y = \epsilon^3 K_1(M_\infty^2-1)^{-\frac{1}{2}}\bar{y}$ and

$$[u, v, w, p] = [1, 0, 0, p_\infty] + \frac{\epsilon^2 C^{\frac{1}{4}}\lambda^{\frac{1}{2}}}{(M_\infty^2-1)^{\frac{1}{4}}}[\bar{u}^{(2)}, \bar{v}^{(2)}(M_\infty^2-1)^{\frac{1}{2}}, \bar{w}^{(2)}, \bar{p}^{(2)}] + \ldots, \tag{2.5}$$

with similar $O(\epsilon^2)$ perturbations of the uniform density and temperature. These yield the supersonic quasi-steady potential-flow equation and main matching conditions, for zero incident wave,

$$(M_\infty^2-1)(\bar{p}^{(2)}_{XX}-\bar{p}^{(2)}_{\bar{y}\bar{y}})-\bar{p}^{(2)}_{ZZ}=0, \tag{2.6a}$$

$$\bar{p}^{(2)}\to 0 \quad \text{as} \quad \bar{y}\to\infty, \tag{2.6b}$$

$$\bar{p}^{(2)}\to P, \quad \frac{\partial\bar{p}^{(2)}}{\partial\bar{y}}\to\frac{\partial^2 A}{\partial X^2} \quad \text{as} \quad \bar{y}\to 0+. \tag{2.6c}$$

Subject to suitable far-field conditions of boundedness, the nonlinear problem for U, V, W, P, A in (2.3*a–e*) is closed, therefore, by the $P-A$ pressure-displacement law implied by (2.6*a–c*) controlling $\bar{p}^{(2)}(X, \bar{y}, Z, \hat{t})$. This law can be expressed in the form of a double integral but the above formulation turns out to be more convenient. Computational solutions of the whole nonlinear three-dimensional unsteady interaction governed by (2.3*a–e*), (2.6*a–c*) would be of much interest as well as nonlinear analysis, as in the subsonic case: see also §5, and we note in addition the recent work by Smith (1988*a*) with regard to the possible finite-time break-up of the nonlinear interactive system.

We turn now to the linearized instability properties, to connect up and compare with previous work. With a relatively small disturbance of order h and a normal-mode decomposition, so that

$$(U, V, W, P, A) = (Y, 0, 0, 0, 0)+\{h(\tilde{U}, \tilde{V}, \tilde{W}, \tilde{P}, \tilde{A})\, E+\text{c.c.}\}+O(h^2), \tag{2.7}$$

with

$$E \equiv \exp[\mathrm{i}(\alpha X-\beta Z-\Omega\hat{t})], \tag{2.8}$$

where α, β are the normalized streamwise and spanwise wavenumbers and Ω is the normalized frequency, the governing equations (2.3*a–c*) reduce to

$$\mathrm{i}\alpha\tilde{U}+\tilde{V}_Y+\mathrm{i}\beta\tilde{W}=0, \tag{2.9a}$$

$$-\mathrm{i}\Omega\tilde{U}+\mathrm{i}\alpha Y\tilde{U}+\tilde{V}=-\mathrm{i}\alpha\tilde{P}+\tilde{U}_{YY}, \tag{2.9b}$$

$$-\mathrm{i}\Omega\tilde{W}+\mathrm{i}\alpha Y\tilde{W}=-\mathrm{i}\beta\tilde{P}+\tilde{W}_{YY}, \tag{2.9c}$$

subject to

$$\tilde{U}=\tilde{V}=\tilde{W}=0 \quad \text{at} \quad Y=0, \tag{2.9d}$$

$$\tilde{U}\to\tilde{A}, \quad \tilde{W}\to 0 \quad \text{as} \quad Y\to\infty. \tag{2.9e}$$

Here the supersonic interaction in (2.6*a*, *b*) yields

$$\bar{p}^{(2)}=h\tilde{P}\exp[-\{\beta^2/(M_\infty^2-1)-\alpha^2\}^{\frac{1}{2}}\bar{y}]\,E+\text{c.c.} \tag{2.10a}$$

provided

$$\mathrm{Re}\{\beta^2/(M_\infty^2-1)-\alpha^2\}^{\frac{1}{2}}>0. \tag{2.10b}$$

Hence the interaction law between $\tilde{P}$ and $\tilde{A}$ is

$$\{\beta^2/(M_\infty^2-1)-\alpha^2\}^{\frac{1}{2}}\tilde{P}=\alpha^2\tilde{A} \tag{2.10c}$$

from (2.6*c*). Following earlier instability analysis (Smith 1979*a*, *b* and references therein) we obtain from (2.9*a–c*) the solution

$$(\alpha\tilde{U}+\beta\tilde{W})_Y=\tilde{B}\,\mathrm{Ai}(\xi): \quad \xi=(\mathrm{i}\alpha)^{\frac{1}{3}}Y+\xi_0, \quad \xi_0=-\mathrm{i}^{\frac{1}{3}}\Omega/\alpha^{\frac{2}{3}}, \tag{2.11a}$$

where Ai denotes the Airy function, $\mathrm{i}^{\frac{1}{3}}=\exp(\mathrm{i}\pi/6)$ and $\tilde{B}$ is an unknown constant, and then the no-slip and displacement conditions require

$$\tilde{B}(\mathrm{i}\alpha)^{\frac{1}{3}}\mathrm{Ai}'(\xi_0)=\mathrm{i}(\alpha^2+\beta^2)\tilde{P}, \tag{2.11b}$$

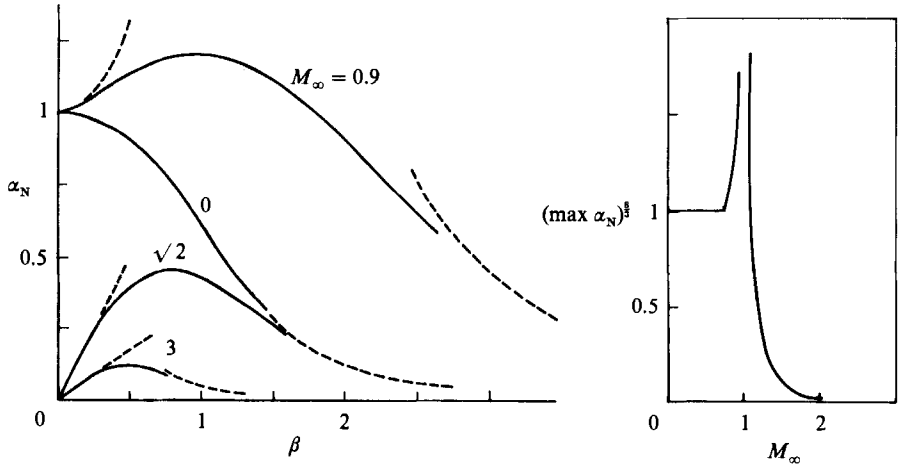

FIGURE 1. Neutral subsonic and supersonic stability, showing the dependence of the neutral wavenumber α_N on the Mach number M_∞ and the spanwise wavenumber β.

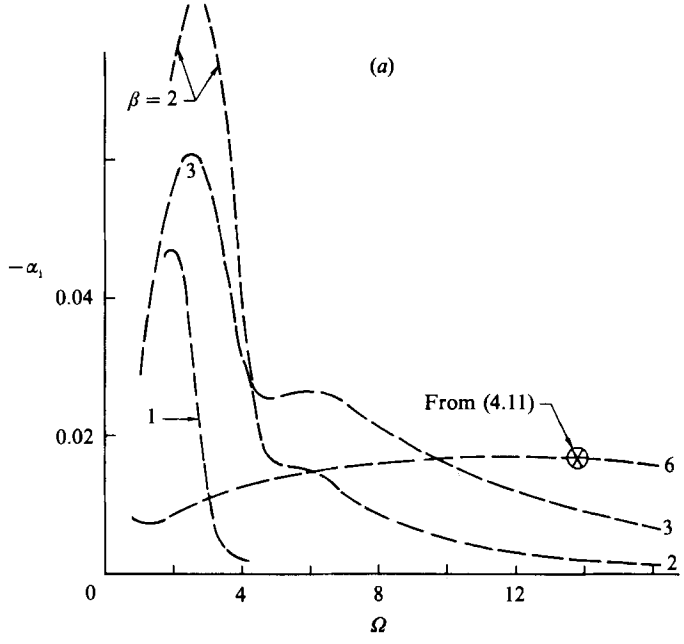

FIGURE 2(a). For caption see facing page.

$$\tilde{B}(\mathrm{i}\alpha)^{-\frac{1}{3}}\kappa(\xi_0) = \alpha\tilde{A} \quad \left[\kappa \equiv \int_{\xi_0}^{\infty} \mathrm{Ai}\,(q)\,\mathrm{d}q\right], \tag{2.11c}$$

in turn. So the combination of (2.10c) and (2.11b, c) gives the eigenrelation

$$(\mathrm{i}\alpha)^{\frac{1}{3}}(\alpha^2+\beta^2) = (\mathrm{Ai}'/\kappa)(\xi_0)\{\beta^2/(M_\infty^2-1)-\alpha^2\}^{\frac{1}{2}} \tag{2.12}$$

between α, β, Ω for normal modes, given the definitions in (2.10b), (2.11a, c).

The next section describes first the *spatial* instability properties, resulting from (2.12) with Ω, β kept real and so α is in general complex, and second the *temporal*

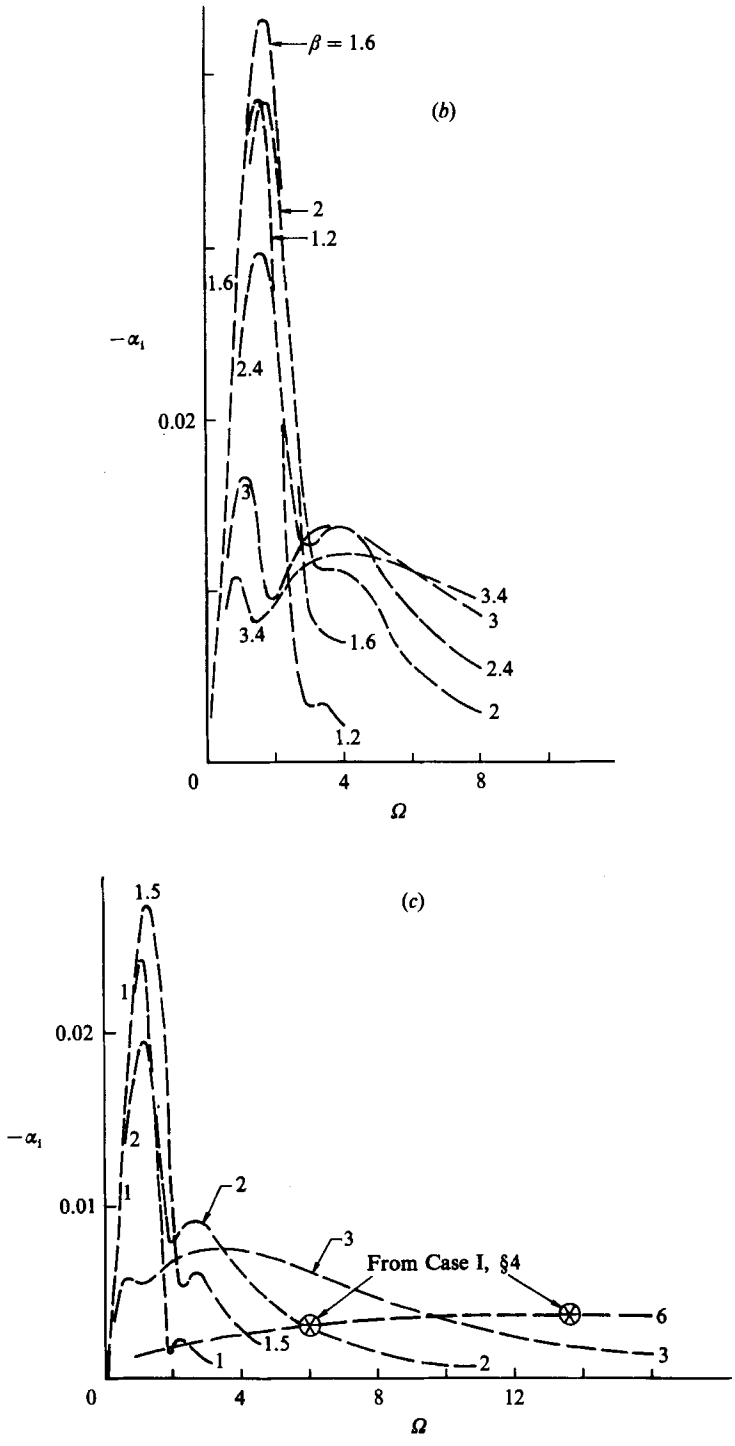

FIGURE 2. Normalized spatial growth rates $-\alpha_i$ versus frequency Ω for various β, and (*a*) $M_\infty = 2$, (*b*) 3, (*c*) 4. Comparisons with the analysis in §4 are also included.

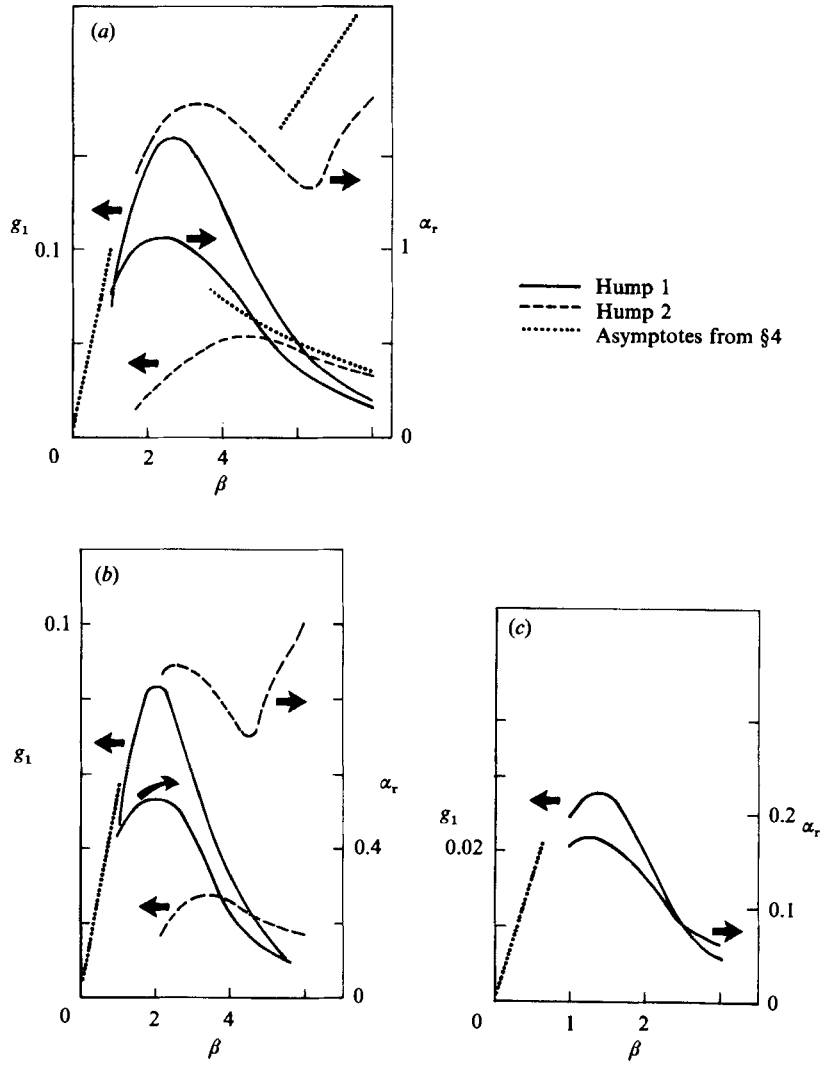

FIGURE 3. Maximum normalized spatial growth rates g_1 versus β at (*a*) $M_\infty = \sqrt{2}$, (*b*) 2, (*c*) 4, for the first and second instability humps, along with comparisons from §4.

instability where α, β are real and Ω is complex. The more general instability problem where β, α are both complex could also be addressed. Again, it is observed that non-parallel-flow effects along the plate are taken into account through the slow dependence on x in the scalings such as (2.2), as in Smith (1979*a*, *b*). We finish this section by noting that the case of neutral stability, where all of α, β, Ω [$= \alpha_N, \beta, \Omega_N$] are real, occurs for

$$\xi_0 = -d_1 \mathrm{i}^{\frac{1}{3}}, \; (\mathrm{Ai}'/\kappa)(\xi_0) = d_2 \mathrm{i}^{\frac{1}{3}}$$

($d_1 \approx 2.3, d_2 \approx 1.0$, see e.g. Drazin & Reid 1981; Miles 1960; Smith 1979*a*, *b*), implying the relation

$$\alpha_N^{\frac{1}{3}}(\alpha_N^2 + \beta^2) = d_2\{\beta^2/(M_\infty^2 - 1) - \alpha_N^2\}^{\frac{1}{2}}, \tag{2.13a}$$

$$\Omega_N = d_1 \alpha_N^{\frac{2}{3}}. \tag{2.13b}$$

The dependence of these neutral conditions on β (here $\beta \geqslant 0$ without loss of

generality), and the corresponding subsonic results, are summarized in figure 1 and can be compared with subsequent computations. The result (2.13*a*) may be expressed conveniently as a quadratic equation for β^2 in terms of α_N, and we observe that neutral waves are confined to the range $\alpha_N^2 \leqslant d_2^2/[4M_\infty^2(M_\infty^2-1)]$. Also, the constraint

$$\alpha < \beta(M_\infty^2-1)^{-\frac{1}{2}} \tag{2.14}$$

holds for neutral or temporal instability/stability waves, in view of (2.10*b*), meaning that the directions of such waves lie *outside* the wave-Mach cones at any particular point. Waves travelling inside the wave-Mach lines by contrast are stable as regards viscous–inviscid first modes and their growth or decay is decided on the $O(1)$ lengthscale in x, where, as mentioned in §§1, 5, non-parallel-flow effects matter considerably.

3. Results and comparisons

The properties of the eigenrelation (2.12) can be found in terms of the Tietjens function, for example as tabulated by Miles (1960), but for computation we preferred to go back and solve the ordinary differential equations (2.9*a–c*) in the form

$$\mathrm{i}\alpha(Y-\Omega/\alpha)\tilde{\tau} = \tilde{\tau}_{YY} \tag{3.1a}$$

for the skewed shear $\tilde{\tau} \equiv (\alpha U+\beta W)_Y$, with

$$\tilde{\tau}_Y(0) = \mathrm{i}(\alpha^2+\beta^2)\tilde{P}, \quad \tilde{\tau}(\infty) = 0, \quad \int_0^\infty \tilde{\tau}\,\mathrm{d}Y = \alpha\tilde{A} \tag{3.1b–d}$$

and with (2.10*c*). Here we converted (3.1*a*) to two first-order equations for $\tilde{\tau}$ and $\tilde{q} \equiv \tilde{\tau}_Y$ and then two-point finite differences were taken in Y, with second-order accuracy. The differenced representation of (3.1*a–d*) was solved as a boundary-value problem for $\tilde{A}/\tilde{P}$ using inversion of a tridiagonal matrix and Newton iteration to satisfy the $\tilde{P}-\tilde{A}$ law (2.10*c*), determining α for a given real Ω, β (spatial stability case) or Ω for real α, β (temporal stability). Grid-size checks were made by performing the calculations on grids of 101×0.1, 201×0.1 and 201×0.05 in Y, the results from which were found to differ hardly at all in the present graphical terms.

Results for *spatial* instability are presented in figures 2–5. In figure 2, α_i values are plotted against real Ω for a number of prescribed values of the spanwise wavenumber β, at representative Mach numbers. Sample checks provided by the limiting cases studied later are also shown. Figure 3 shows a sample of the corresponding maximum normalized growth rates $-\alpha_i = g_1(\beta, M_\infty)$ resulting from the calculations such as in figure 2, as functions of β, M_∞. For each Mach number M_∞ the values $\alpha_r = \alpha_1$, $\beta = \beta_1$ at which g_1 is maximum can be deduced and hence the obliqueness angle $\theta_1 \equiv \tan^{-1}(\beta_1/\alpha_1)$ of maximum normalized growth rate is found, as a function of Mach number, as presented in figure 4 along with other main quantities. Comparisons with Mack's (1975, 1984, 1986) predictions for $R(=Re^{\frac{1}{2}}) = 1500$ are made in figure 5. The agreement found, although not especially close at the larger Mach numbers for reasons given subsequently, is not unreasonable, particularly in view of the various limitations present, as discussed in §5 below: for example, the TS limitations (2.14) and (5.4) below [or (1.2) above], requiring $\theta_1 > \tan^{-1}\{(M_\infty^2-1)^{\frac{1}{2}}\}$ (an inviscid criterion) and $M_\infty \ll R^{\frac{1}{5}}$ in turn according to the present theory, are both violated by the finite-Reynolds-number computations as M_∞ increases and as θ_1 dips below the

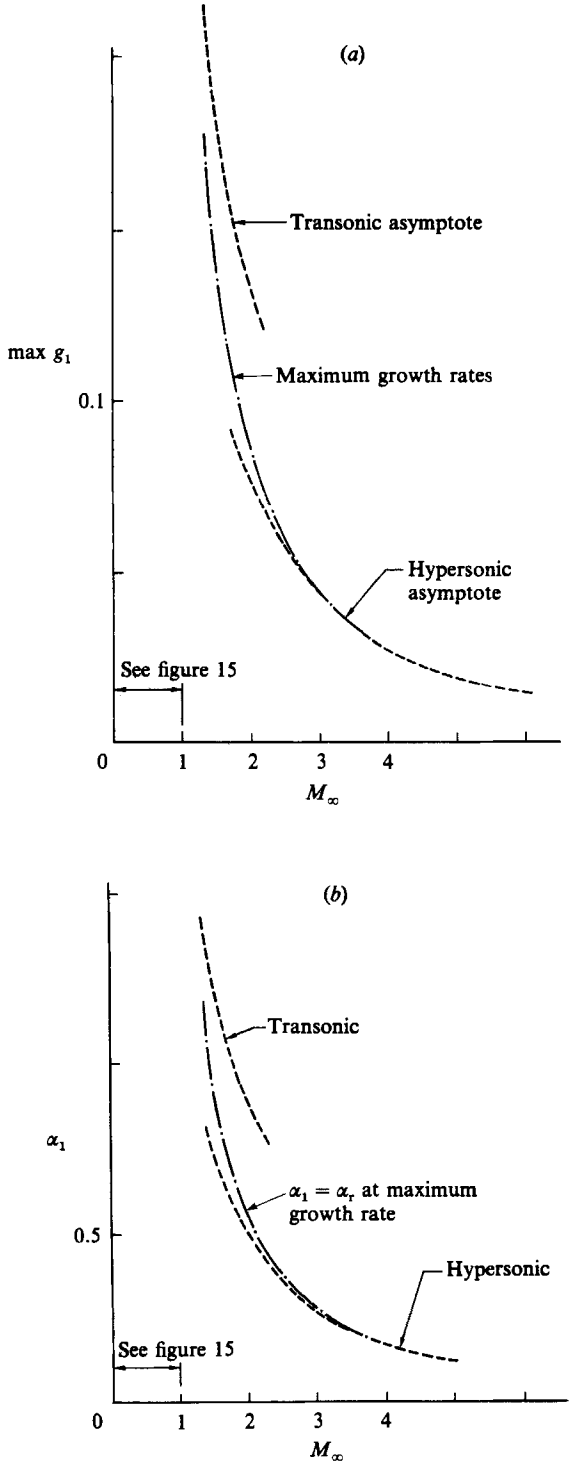

FIGURE 4(*a*, *b*). For caption see facing page.

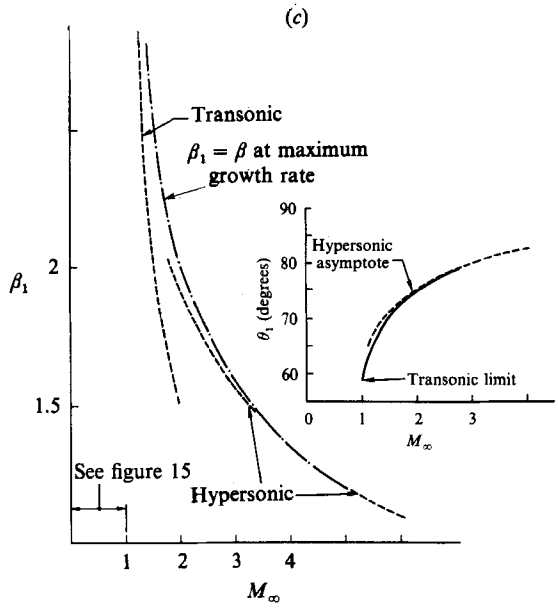

FIGURE 4. Maximum normalized spatial growth rates. (*a*) Growth rates (max g_1), (*b*) corresponding streamwise wavenumbers α_1, (*c*) corresponding spanwise wavenumbers β_1 and wave angles θ_1, versus M_∞. The transonic and hypersonic limits from §4 are also shown.

inviscid cut-off curve. Again, the major differences in growth-rate† predictions occur during the higher-M_∞ regime, further suggesting the increasing impact of the restriction (5.4) [or (1.2)] there on the Orr–Sommerfeld calculations.

A similar treatment applies for *temporal* instability as shown in figures 6–9. Figure 6 displays graphs of the growth rate Ω_i versus real α for various β values, at two sample Mach numbers M_∞. Figure 7 then shows the maxima $g_2(\beta, M_\infty)$ of the normalized temporal growth rates *vs.* β at various Mach numbers, with figure 8 giving the resulting dependence on Mach number of the maximum normalized growth rate, i.e. $\max g_2$, and the obliqueness angle $\theta_2 \equiv \tan^{-1}(\beta_2/\alpha_2)$ for that maximum temporal growth rate, achieved at $\alpha = \alpha_2, \beta = \beta_2$, say. Comparisons with Mack's (1975, 1984, 1986) results as shown in figure 9 are again not unreasonably close and seem not too discouraging at this stage especially in view of the comments and criticisms given in the previous paragraph and in §5.

Apart from the not too large disagreements with the Orr–Sommerfeld computations and their explanations above via (2.14) and (5.4) a number of other notable features arise in the results above. These are principally the double-hump formation in the growth-rate curves in figures 2 and 6 for increased β and the behaviour of the solutions in the extremes of Mach number, $M_\infty \to \infty$ and $M_\infty \to 1\pm$. These motivate the work in the next section.

† The growth rates here are given by $G \propto g_1/\epsilon^3 K_1$, with K_1 defined in (2.1*c*) bringing in the extra Mach-number and temperature-ratio dependence.

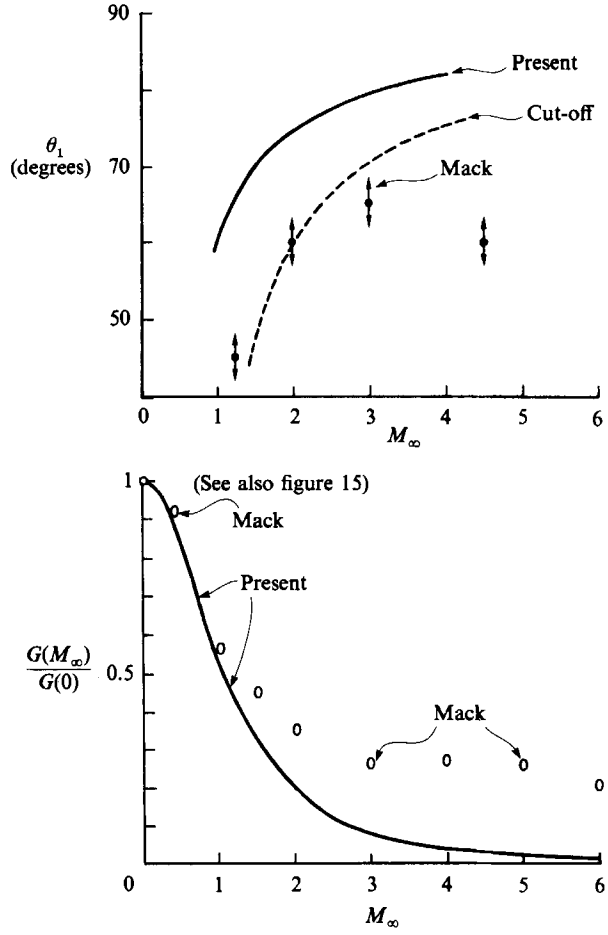

FIGURE 5. Comparisons with Mack's (1975, 1984, 1986) computational results, for an insulated wall, at local Reynolds number $R = 1500$. The dashed curve shows the lower limit in θ_1 according to the cut-off criterion (2.14).

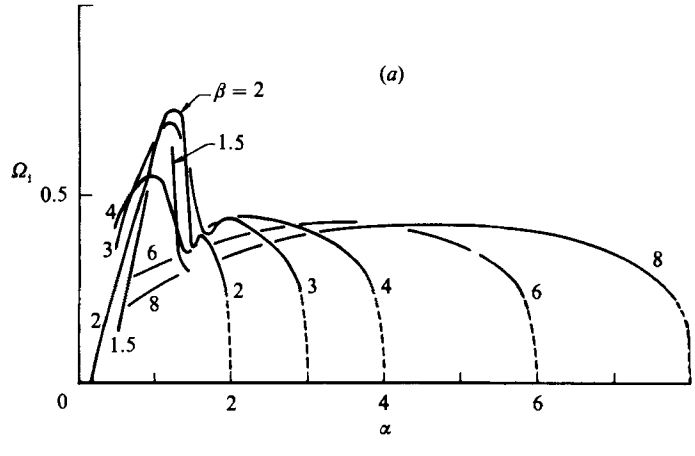

FIGURE 6(a). For caption see facing page.

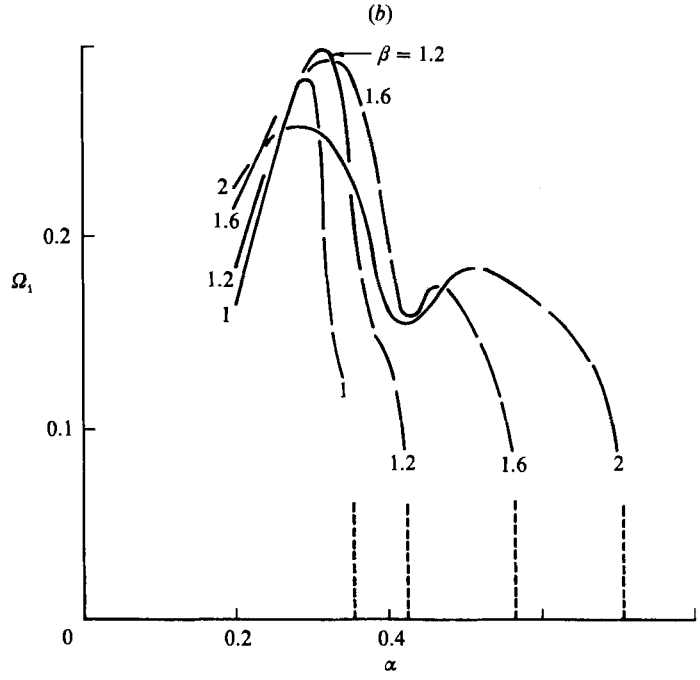

FIGURE 6. Temporal normalized growth rates and analytical comparisons. (*a*) $M_\infty = \sqrt{2}$, (*b*) 3. Dashed curves are from Case IV, §4.

4. Limiting cases: extreme wavenumbers, transonic flows, and hypersonic flows

Here we investigate certain limiting cases of concern, partly to check the computational results and partly to indicate some further interesting developments. Hypersonic ($M_\infty \gg 1$) and transonic ($M_\infty \to 1$) flows are considered as Cases I and II below, followed by extreme spanwise wavenumbers (Case III), the cut-off (Case IV), high frequencies as Case V and the second-hump formation as Case VI. For definiteness we concentrate mostly on supersonic spatial instability, although the temporal and subsonic cases are quite similar and their corresponding results are used in certain figures.

Case I: *hypersonic flow* Here $M_\infty \gg 1$ and the instability properties as given by (2.12) take on an intriguing character. The main features revolve around the small regime where

$$(\alpha, \beta, \Omega) \sim (M_\infty^{-\frac{3}{2}}\tilde{\alpha}, M_\infty^{-\frac{1}{2}}\tilde{\beta}, M_\infty^{-1}\tilde{\Omega}) + \ldots, \tag{4.1}$$

for $\tilde{\alpha}, \tilde{\beta}, \tilde{\Omega}$ of $O(1)$, and (2.12) reduces to the form

$$\mathrm{i}^{\frac{1}{3}}\tilde{\alpha}^{\frac{1}{3}}\tilde{\beta}^2 = (\mathrm{Ai}'/\kappa)(\tilde{\xi}_0)(\tilde{\beta}^2 - \tilde{\alpha}^2)^{\frac{1}{2}}, \quad \tilde{\xi}_0 \equiv -\mathrm{i}^{\frac{1}{3}}\tilde{\Omega}\tilde{\alpha}^{-\frac{2}{3}}. \tag{4.2}$$

The major physical difference here is that the streamwise pressure gradient $\partial P/\partial X \propto \mathrm{i}\alpha\tilde{P}$ becomes negligible in the lower deck, with the wave angle shifting close to 90° and the length and time scales all increasing. The solutions for the hypersonic limit (4.2) are displayed in figure 10 (see also figure 7*d* in the temporal case) and confirm that the maximum growth rate is captured by the regime (4.1). As $\tilde{\beta}$ increases the growth rate $-\tilde{\alpha}_i$ eventually falls. In addition the double-hump formation comes back into play, as can be verified by analysis of (4.2) for large $\tilde{\beta}$, analogous to the

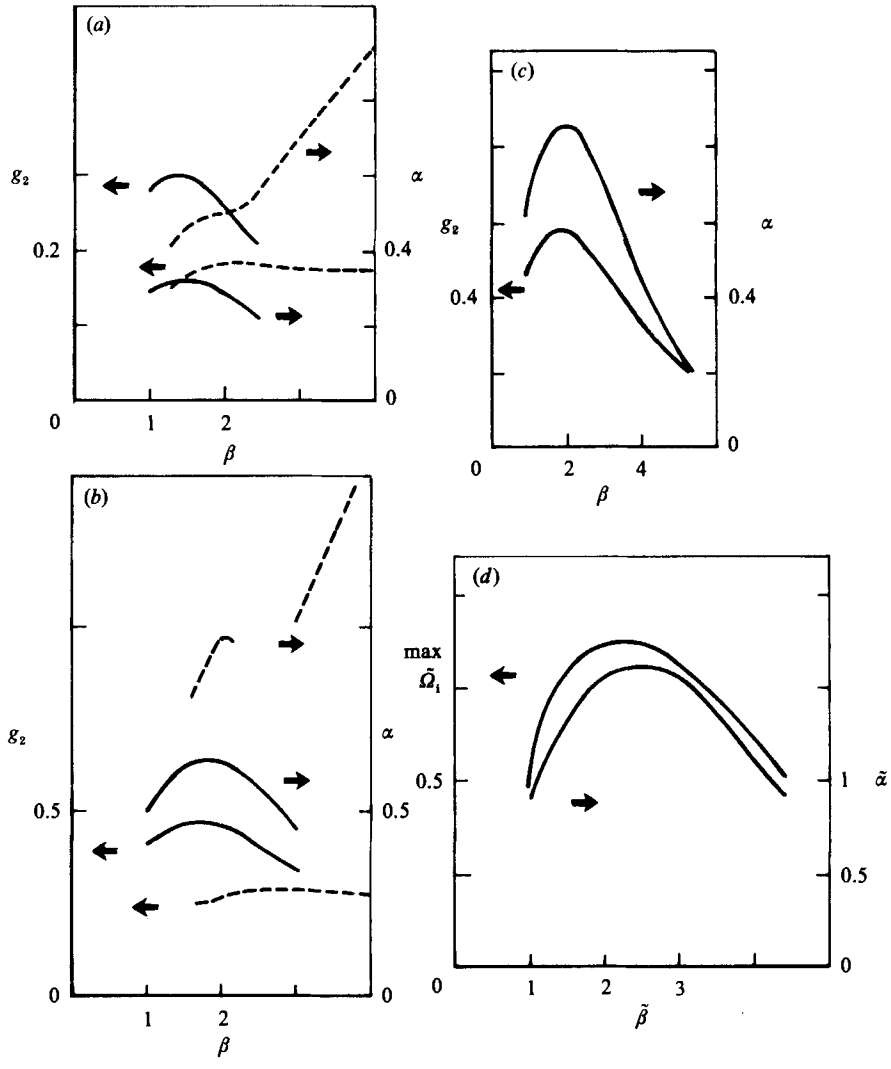

FIGURE 7. Maximum normalized temporal growth rates g_2 versus β, for the first and second instability humps at (*a*) $M_\infty = 3$, (*b*) 2, (*c*) 1.7, (*d*) $\to \infty$.

second-hump analysis for $O(1)$ values of β given in the next paragraph. For small $\tilde{\beta}$, on the other hand,

$$\tilde{\alpha} \sim \tilde{\beta} - \tilde{\beta}^{\frac{11}{3}}\tilde{\alpha}_1 + \ldots, \quad \Omega = \tilde{\beta}^{\frac{2}{3}}\tilde{\Omega}_0, \tag{4.3a}$$

predominantly, where from (4.2) $\tilde{\alpha}_1$ is given by

$$2\tilde{\alpha}_1 = [\mathrm{i}^{\frac{1}{3}}(\kappa/\mathrm{Ai}')(\tilde{\xi}_0)]^2, \quad \tilde{\xi}_0 = -\mathrm{i}^{\frac{1}{3}}\tilde{\Omega}_0, \tag{4.3b}$$

so that again the growth rate $-\tilde{\alpha}_i$ tends to zero. The results (4.3*a*, *b*) are in accord with (2.13) at the neutral condition where $\tilde{\alpha}_{1i} = 0, \tilde{\Omega}_0 = d_1$, and also with Case V below for large $\tilde{\Omega}_0$.

The presence of the second mound of instability can be inferred from (4.2) for large $\tilde{\beta}$, or, as a more general alternative, from completely examining $O(1)$ values of β when

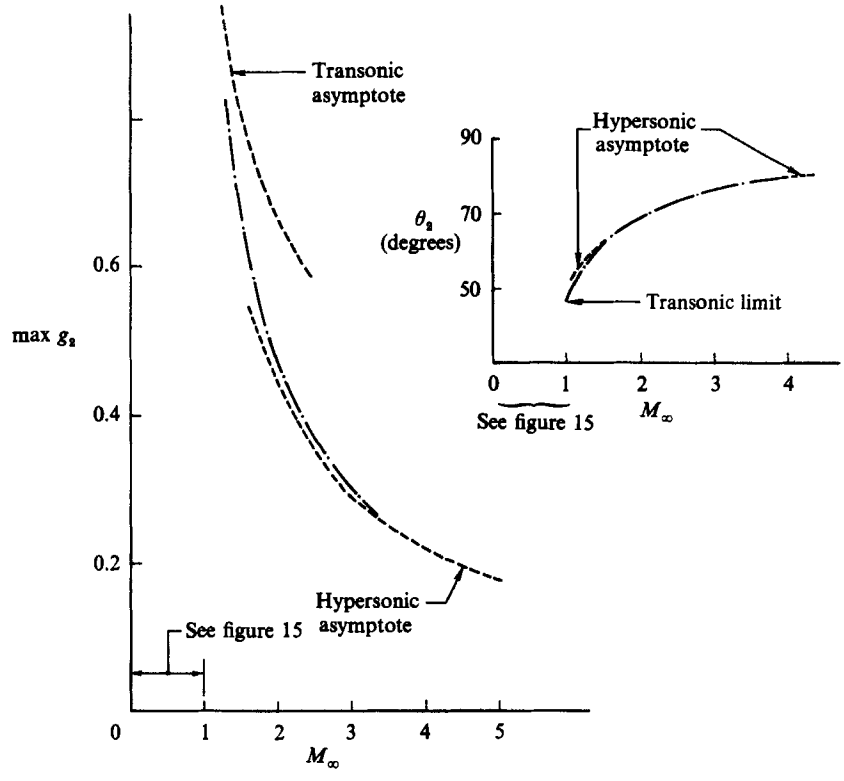

FIGURE 8. Maximum normalized temporal growth rates ($\max g_2$) versus Mach number (plus obliqueness angles (θ_2) and the transonic and hypersonic limits from §4).

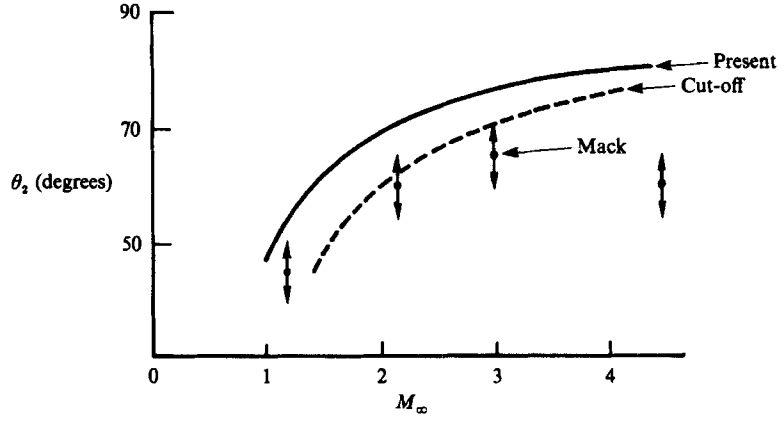

FIGURE 9. Comparisons with Mack's (1975, 1984, 1986) computational results at $R = 1500$, for an insulated wall. The dashed curve is as in figure 5.

$M_\infty \gg 1$ (the two processes are found to match) as follows. At small $\Omega \sim M_\infty^{-2}\hat{\Omega}$, $\alpha \sim M_\infty^{-3}\hat{\alpha}$, for β of order unity, and so

$$\mathrm{i}^{\frac{1}{3}}\hat{\alpha}^{\frac{1}{3}}\beta = (\mathrm{Ai}'/\kappa)(\hat{\xi}_0), \hat{\xi}_0 \equiv -\mathrm{i}^{\frac{1}{3}}\hat{\Omega}\hat{\alpha}^{-\frac{2}{3}} \tag{4.4}$$

from (2.12). Neutrality occurs at finite $\hat{\Omega}, \hat{\alpha}$, the growth rate is then positive for

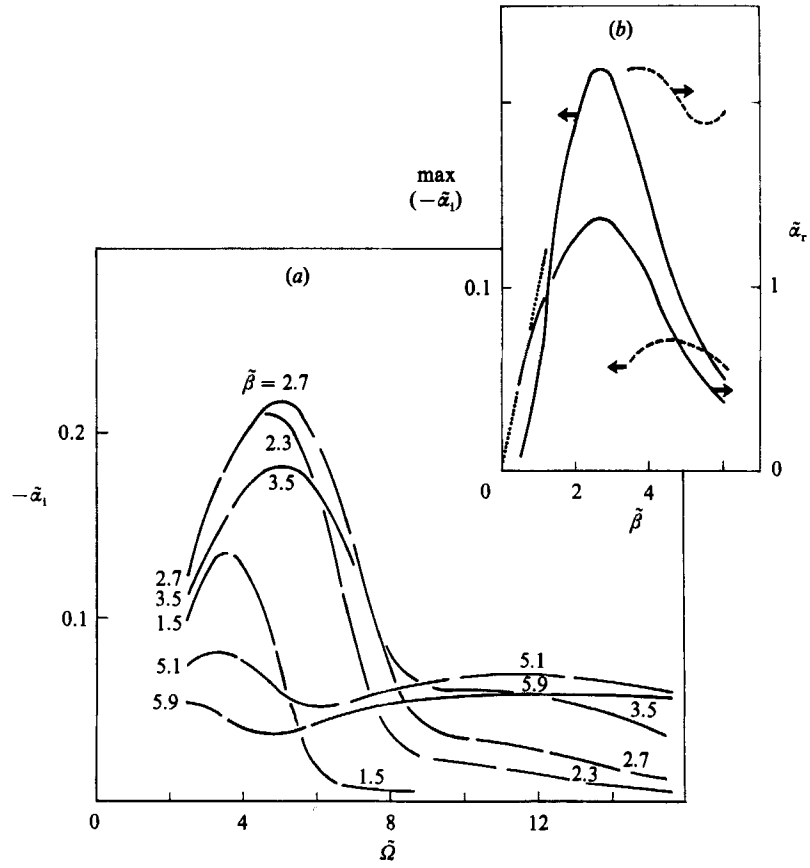

FIGURE 10. The hypersonic limit, from Case I of §4, showing the spatial growth rates and their maxima.

higher $\hat{\Omega}$, but as $\hat{\Omega} \to \infty$ the growth rate continues to increase. This follows from inserting the asymptote

$$(\mathrm{Ai}'/\kappa)(\xi_0) \sim -\xi_0 - \xi_0^{-\frac{1}{2}} \quad \text{as} \quad \xi_0 \to -\mathrm{i}^{\frac{1}{3}}\infty \tag{4.5}$$

into (4.4), which yields the results

$$\hat{\alpha}_r \sim \hat{\Omega}/\beta, \quad -\hat{\alpha}_i \sim \hat{\Omega}^{\frac{1}{2}}/\sqrt{2\beta^2} \quad (\hat{\Omega} \gg 1). \tag{4.6a}$$

A second stage therefore takes place, at frequencies Ω increased to $O(1)$, in which

$$\alpha = M_\infty^{-1}\hat{\alpha}_0 + M_\infty^{-2}\hat{\alpha}_1 + \ldots \tag{4.6b}$$

and, from substitution into (2.12), we obtain the relations

$$\hat{\alpha}_0\beta^2 = \Omega(\beta^2 - \hat{\alpha}_0^2)^{\frac{1}{2}}, \tag{4.6c}$$

$$\hat{\alpha}_1 = \Omega^{-\frac{3}{2}}\hat{\alpha}_0^2(\beta^2 - \hat{\alpha}_0^2)\beta^{-2}\exp(-\tfrac{3}{4}\pi\mathrm{i}), \tag{4.6d}$$

fixing $\hat{\alpha}_0$ (real), $\hat{\alpha}_1$ (complex) in turn, for given $O(1)$ values of β, Ω. The relations (4.6c, d) confirm the structure of the second hump during the current stage since $-\hat{\alpha}_{1i} \to 0+$ at the two extremes of small and large Ω, matching (4.6a) and the cut-off, Case IV below, respectively. The graphs of $\hat{\alpha}_0, \hat{\alpha}_1$ versus Ω are drawn in figure 11.

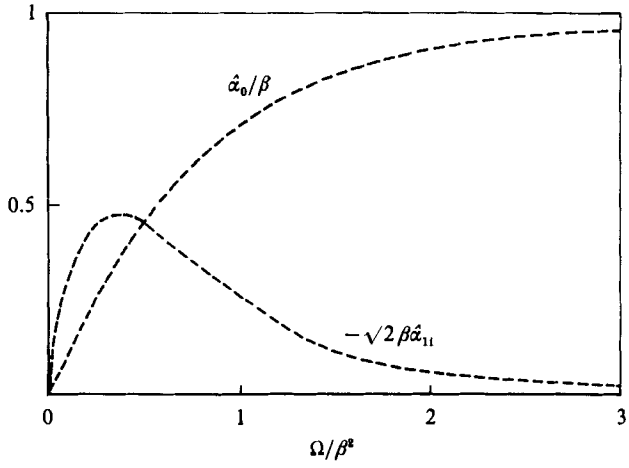

FIGURE 11. The second hump of instability in hypersonic flow, from (4.6*c*, *d*).

Further, the maximum growth rate from this second hump occurs when $\hat{\alpha}_0 = (\hat{\alpha}_0)_{\max}$, $\Omega = \Omega_{\max}$, where

$$(\hat{\alpha}_0)_{\max} = \beta/2\sqrt{2}, \quad \Omega_{\max} = \beta^2/\sqrt{7}, \tag{4.7a}$$

giving the maximum

$$(-\hat{\alpha}_{1i})_{\max} = 7^{\frac{7}{4}}/[2^{\frac{13}{2}}\beta]. \tag{4.7b}$$

Thus the main instability predictions for the second hump, at large M_∞, may be expressed as

$$(\alpha_r)_{\max} = \frac{\beta}{2^{\frac{3}{2}}M_\infty}, \quad (-\alpha_i)_{\max} = \frac{7^{\frac{7}{4}}}{2^{\frac{13}{2}}\beta M_\infty^2}, \quad \Omega_{\max} = \frac{\beta^2}{\sqrt{7}}, \tag{4.7c}$$

which apply for $\beta^2 M_\infty \gg 1$ (equivalent to $\tilde{\beta} \gg 1$). Comparisons of (4.7*c*) and (4.2) with the earlier computations (spatial and temporal) are shown in some of the earlier figures and are seen to be very favourable even at moderate Mach numbers.

Further repercussions from the hypersonic limit are discussed in §5.

Case II: *transonic flow* When $M_\infty \to 1+$ and the transonic regime is approached, the principal area of concern centres on

$$(\alpha, \beta, \Omega) = (m^{-\frac{3}{4}}\alpha^*, m^{-\frac{3}{4}}\beta^*, m^{-\frac{1}{2}}\Omega^*) + \ldots, \tag{4.8a}$$

where the maximum growth rate occurs. Here $\alpha^*, \beta^*, \Omega^*$ are $O(1)$ and $m \equiv (M_\infty^2 - 1)^{\frac{1}{2}}$ is small, so that (2.12) reduces to the relation

$$(\mathrm{i}\alpha^*)^{\frac{1}{3}}(\alpha^{*2} + \beta^{*2}) = (\mathrm{Ai}'/\kappa)(\xi_0^*)\beta^*, \quad \xi_0^* \equiv -\mathrm{i}^{\frac{1}{3}}\Omega^*/\alpha^{*\frac{2}{3}}, \tag{4.8b}$$

giving the results in figure 12. Essentially, the streamwise pressure gradient $\partial P/\partial X$ is now negligible in the upper deck: cf. hypersonic flow in Case I. The transonic-limit prediction (4.8*b*) agrees well with the earlier results as M_∞ falls: see the figures. For small β^*, the solution of (4.8*b*) focuses around $\alpha^* \propto \beta^{*\frac{3}{7}}, \Omega^* \propto \beta^{*\frac{2}{7}}, \xi_0^* \sim 1$, to provide a merging with the extra regime noted later. As β^* increases the scaled growth rate $-\alpha_i^*$ attains its overall maximum, the double hump of instability appears and eventually the second hump begins to dominate at larger β^* values. This is supported by a large-β^* analysis which, using (4.5), shows that

$$\alpha^* \sim \beta^* \alpha_0^* + \beta^{*-1}\alpha_1^*, \quad \Omega^* \sim \beta^{*2}\Omega_0^* \quad (\text{for } \beta^* \gg 1). \tag{4.9a}$$

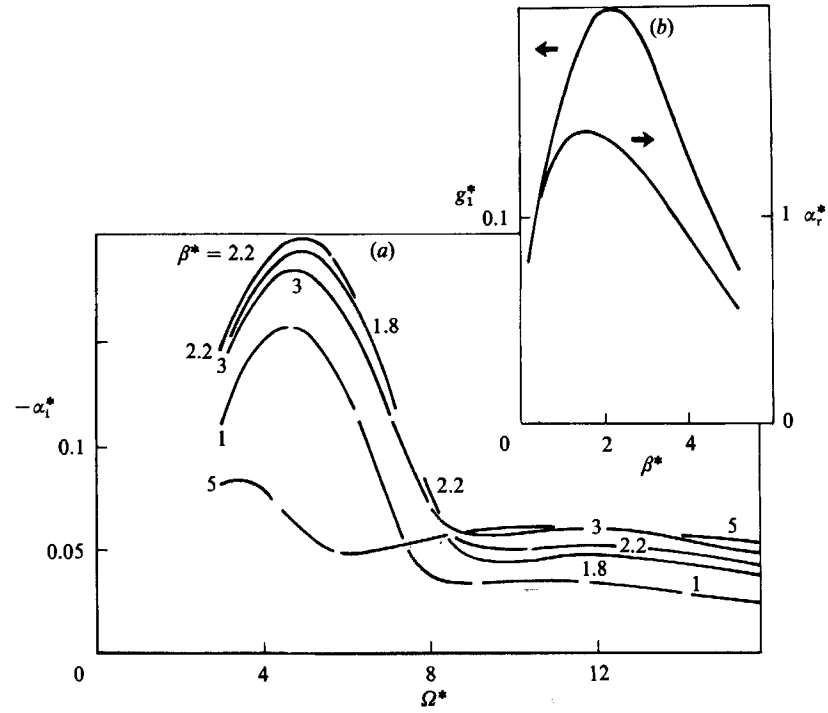

FIGURE 12. The major transonic limit, from (4.8*b*), showing the spatial growth rates and their maxima.

Here α_0^* (real), α_1^* (complex) are given by

$$\alpha_0^*(\alpha_0^{*2}+1) = \Omega_0^*, \tag{4.9b}$$

$$\alpha_1^* = \alpha_0^{*2}\exp(-\tfrac{3}{4}\pi\mathrm{i})/\Omega_0^{*\frac{1}{2}}(2\alpha_0^{*3}+\Omega_0^*) \tag{4.9c}$$

in turn, as shown in figure 12. The maximum growth rate for this second hump is encountered when $\alpha_0^{*2} = [2\sqrt{10}-5]/15$, giving the values

$$\alpha_0^* = 0.29716, \quad -\alpha_{1i}^* = 0.29211, \quad \Omega_0^* = 0.32340 \text{ (at max.)}. \tag{4.9d}$$

Hence the general prediction for the second hump, as $M_\infty \to 1+$, is

$$(\alpha_r)_{\max} = \beta\alpha_0^*, \quad (-\alpha_i)_{\max} = \frac{(-\alpha_{1i}^*)\beta^{-1}}{(M_\infty^2-1)^{\frac{3}{4}}}, \quad \Omega_{\max} = \beta^2\Omega_0^*(M_\infty^2-1)^{\frac{1}{2}}, \tag{4.9e}$$

along with the numerical values in (4.9*d*), provided $\beta \gg (M_\infty^2-1)^{-\frac{3}{8}}$. The predictions (4.9*e*) for the transonic limit (second hump) again agree well with the earlier calculations at smaller M_∞ values, as the figures indicate.

An extra, distinct, regime is also present at much smaller spanwise wavenumbers β, we note, where α, Ω are $O(1)$ but $\beta \sim m\beta_0$ with β_0 of $O(1)$, thus reducing (2.12) to the eigenrelation

$$\mathrm{i}^{\frac{1}{3}}\alpha^{\frac{7}{3}} = (\mathrm{Ai}'/\kappa)(\xi_0)(\beta_0^2-\alpha^2)^{\frac{1}{2}}. \tag{4.10}$$

For these transonic modes the spanwise pressure gradient $\partial P/\partial Z$ has a diminished role in the lower deck and the typical wave angle is small, of order m. This regime is fairly minor, however, as it yields a one-hump instability curve (figure 13) with maximum growth rate $-\alpha_i$ only of order unity as opposed to the large $O(m^{-\frac{3}{4}})$ growth

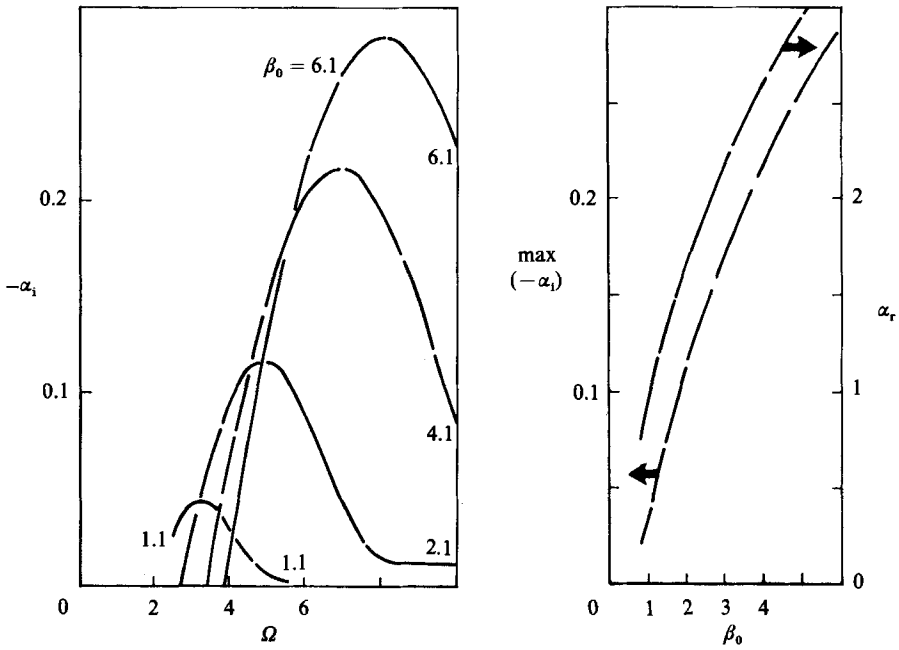

FIGURE 13. The minor transonic limit (4.10), which approaches the major one of figure 12 as β becomes large.

rates holding in the regime of (4.8*b*). Again, as Ω becomes large $\alpha_r \to \beta_0 -$, $\alpha_i \to 0$ and the cut-off description in Case IV below comes into force.

Case III: *extreme spanwise wavenumbers* We address first here the properties of (2.12) when the spanwise wavenumber β is large, for general Mach numbers. The asymptote (4.5) implies that the strongest effect then arises at the higher frequencies where

$$\alpha = \beta\alpha_0 + \beta^{-1}\alpha_1 + \ldots, \quad \Omega = \beta^2\Omega_0, \tag{4.11a}$$

with α_0 (real), α_1 (complex), Ω_0 (real) all of order unity. Substituting into (2.12) we find the results, using $m^2 \equiv M_\infty^2 - 1$ again,

$$\alpha_0(1+\alpha_0^2) = \Omega_0[1/m^2 - \alpha_0^2]^{\frac{1}{2}}, \tag{4.11b}$$

$$\alpha_1 = \alpha_0^2\Omega_0^{-\frac{3}{2}}\exp(-\tfrac{3}{4}\pi\mathrm{i})(1+\alpha_0^2)(1/m^2-\alpha_0^2)/[(3\alpha_0^2+1)/m^2 - 2\alpha_0^4], \tag{4.11c}$$

controlling α_0, α_1. Since $-\alpha_{1i} \to 0+$ at the two ends $\Omega_0 \to 0$ (where $\alpha_0 \sim \Omega_0/m$) and $\Omega_0 \to \infty$ (where $\alpha_0 \to m^{-1}+$) the maximum growth rate here occurs at an $O(1)$ value of Ω_0, thus capturing the second hump of instability. This is drawn in figure 14. The limiting predictions (4.11*a–c*) for the second hump are compared with the previous computations in certain of the earlier figures and the agreement is seen to be very good at the larger β values.

In addition, (4.11*a–c*) agree with (4.9*a–c*) for the transonic flow at small m and with (4.6*b–d*) for the hypersonic case at large m.

The second extreme to consider is that of small β, again with general $O(1)$ Mach numbers. This extreme is covered in fact by the formula (4.13*c*) below, governing the cut-off stage, Case IV, since the formula applies for $\beta \to 0$ with the other parameters M_∞, Ω kept fixed. That trend for decreasing β is in good agreement with the computational results of §3.

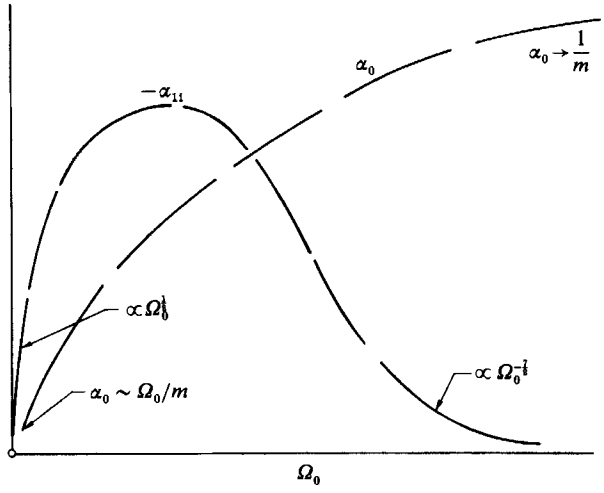

FIGURE 14. Sketch of the main properties of the second hump of instability in supersonic flow, for large β, from (4.11*a–c*).

Case IV: *the cut-off* A cut-off happens when α approaches the upper constraint β/m of (2.14) and this is considered here for general values of β, M_∞, although the cut-off does enter in other circumstances such as in Case III above. Generally, as $\alpha \to \beta/m-$, the frequency $\Omega \to \infty$ and $|\xi_0| \to \infty$, with

$$\alpha = \beta/m - \tilde{\sigma} + \tilde{\sigma}^{\frac{7}{4}}\tilde{\alpha}_1 + \ldots, \quad \Omega = \tilde{\sigma}^{-\frac{1}{2}}\tilde{\Omega}_0, \tag{4.12}$$

where $\tilde{\sigma}$ is small and real. So (2.12) with (4.5) leads to the successive relations

$$\sqrt{2}\tilde{\Omega}_0 = M_\infty^2(m/\beta)^{-\frac{5}{2}}, \quad m\tilde{\alpha}_1 = 2\tilde{\Omega}_0^{-\frac{3}{2}}\beta \exp(-\tfrac{3}{4}\pi i), \tag{4.13a, b}$$

fixing $\tilde{\Omega}_0, \tilde{\alpha}_1$ respectively. The cut-off is governed therefore by the behaviour

$$\alpha \sim \beta/m - \frac{M_\infty^4(\beta/m)^5}{2\Omega^2} + \frac{M_\infty^4(\beta/m)^6 \exp(-\frac{3}{4}\pi i)}{\Omega^{\frac{7}{2}}} + \ldots, \tag{4.13c}$$

which applies for the range $\Omega \gg 1$ usually but for other ranges when M_∞ and/or β takes an extreme value. The main trends from (4.13*c*),

$$\alpha_r \sim \beta/m - \frac{M_\infty^4(\beta/m)^5}{2\Omega^2}, \quad -\alpha_i \sim \frac{M_\infty^4(\beta/m)^6}{\sqrt{2}\Omega^{\frac{7}{2}}}, \tag{4.14a}$$

are in agreement with the computations as Ω increases, as the previous figures show. The corresponding trends near cut-off for temporal instability can also be deduced from (4.13*c*) and give $\Omega_r \to \infty, \Omega_i \to 0$ in the form

$$\Omega_r \sim (\tfrac{1}{2}M_\infty^4)^{\frac{1}{2}}(\beta/m)^{\frac{5}{2}}(\beta/m-\alpha)^{-\frac{1}{2}}, \quad \Omega_i \sim (\tfrac{1}{2}m/\beta)^{\frac{1}{4}}M_\infty^{-1}(\beta/m-\alpha)^{\frac{1}{4}} \tag{4.14b}$$

as $\alpha \to \beta/m$ from below, with α real, and again the agreement with the numerical work of §3 is seen to be good in the temporal-instability figures as α approaches its maximum value β/m.

Case V: *high-frequency waves* For most Mach numbers, high-frequency waves where $\Omega \gg 1$ are associated with relatively small growth rates as given by (4.13*c*) but

high wave speeds and wavenumbers lying outside the range of (4.13*c*) also exist. Generally for $\Omega \gg 1$ we may take

$$(\alpha, \beta) = \Omega^{\frac{1}{2}}(\alpha_0, \beta_0) + \Omega^{-\frac{1}{2}}(\alpha_1, \beta_1) + \ldots, \tag{4.15}$$

for the $O(1)$ wave angles which are of most interest, and then (2.12) gives the results (cf. (4.11))

$$\alpha_0(\alpha_0^2 + \beta_0^2) = (\beta_0^2/m^2 - \alpha_0^2)^{\frac{1}{2}}, \tag{4.16a}$$

$$\alpha_1 \alpha_0\{2m^2 \alpha_0^4(\alpha_0^2 + \beta_0^2) + \beta_0^2\} + \beta_0 \alpha_0^2 \beta_1\{2m^2 \alpha_0^2(\alpha_0^2 + \beta_0^2) - 1\} = (\alpha_0^2 + \beta_0^2)^2 m^2 \alpha_0^5 \exp(-\tfrac{3}{4}\pi \mathrm{i}), \tag{4.16b}$$

controlling α_0 (real), α_1 (complex) as β_0, β_1 vary. These are the supersonic-flow analogues of the eigenrelations used in the nonlinear high-frequency theory of Smith (1985, 1986), Smith & Stewart (1987) for an incompressible boundary layer. In contrast, high-frequency waves for smaller spanwise wavenumbers β such as β of $O(1)$ are governed by the cut-off analysis in Case IV above which leads to (4.13*c*); indeed, as a check, the results (4.16*a*, *b*) tend towards (4.13*c*) as β_0 is reduced and then $\alpha_0 \to \beta_0/m$, indicating the cut-off arising at reduced wavenumbers as required.

Case VI: the second instability mounds We conclude this section by commenting further on the features of the second humps of instability found computationally and analytically. These humps dominate the growth-rate response at the larger spanwise wavenumbers β, for arbitrary Mach numbers, as well as dominating at most β for large Mach numbers for instance. Their character is inviscid to leading order but viscous–inviscid interaction is still necessary to produce the relatively small growth rates present at higher order. The second instability humps are very amenable to analysis, as in Cases I–III above, and so while the first humps are found to produce the overall maximum in the linear growth rates at a given Mach number, the second humps may well allow more progress to be made on the nonlinear front (as an alternative to full computations of the nonlinear system (2.3), (2.6)) and thus may yield somewhat more insight into the compressible transition process.

5. Further comments

The structural approach set out in §2 provides the rational basis for the first modes of instability in the supersonic boundary layer (see also the subsonic version below) and confirms their viscous–inviscid interactive nature, typical of Tollmien–Schlichting waves. It is now well accepted that in general only the underlying assumption of the Reynolds number *Re* being large can make the parallel-flow approximation valid in strict terms, as distinct from its use in the Orr–Sommerfeld approach at finite *Re*. This is for the (unstable) three-dimensional supersonic waves directed outside of the local wave-Mach cones (see (2.14)), of course, whereas the three- and two-dimensional viscous–inviscid waves less obliquely inclined, if unstable, have streamwise lengthscales of $O(1)$ and so are always non-parallel-flow modes, a feature which, again strictly, renders the previous Orr–Sommerfeld results for these first modes invalid even at large *Re*. Further work on these non-parallel less oblique modes is in progress by R. I. Bowles at University College London. Again, the agreement between the present treatment and previous results, for the appropriately oblique first modes, is fairly good in qualitative terms, as regards the wave angle of maximum growth for instance, and it may prove helpful to extend the comparisons, e.g. to precise values of the growth rates, perhaps using further terms

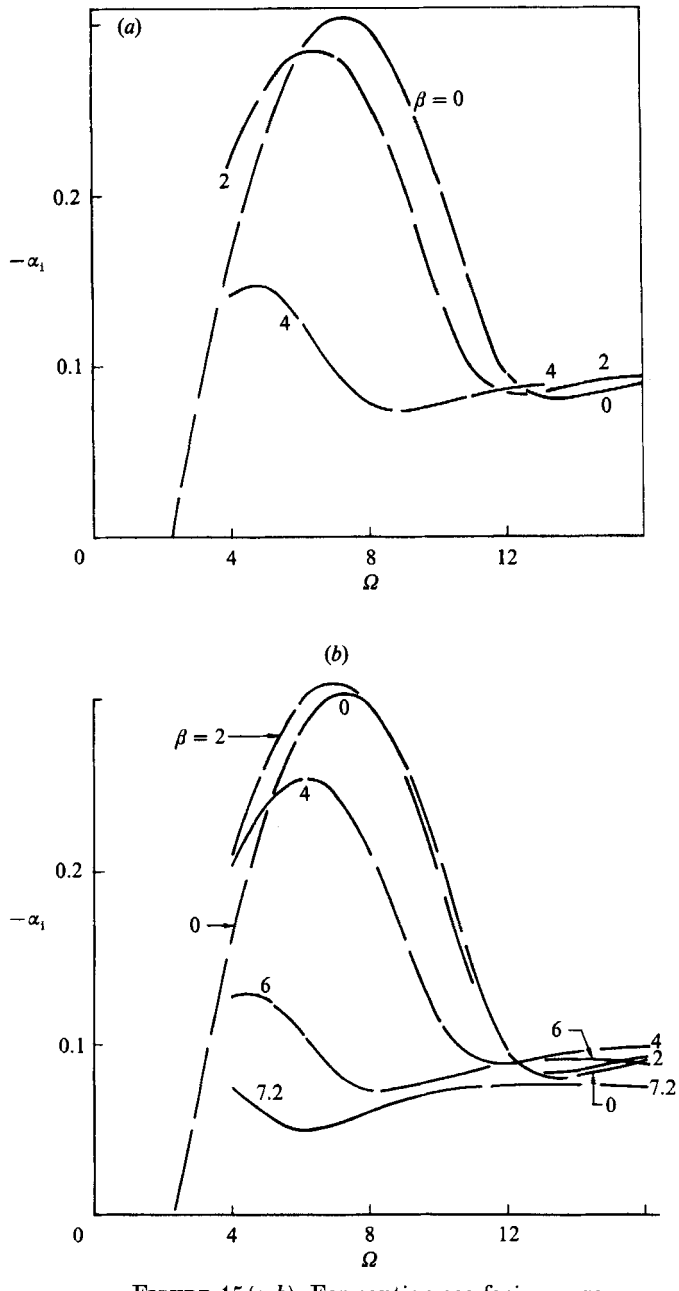

FIGURE 15(*a*, *b*). For caption see facing page.

in the asymptotic series as in Smith (1979*a*, *b*). Another type of numerical extension also seems called for, however, namely to an unsteady interacting-boundary-layer or related method at finite *Re*, for which the present approach provides some more encouragement.

The triple-deck structure used describes only the *first* mode, whereas the *second* mode, a shorter-scale predominantly inviscid one unhindered by non-parallelism, tends to dominate in terms of spatial or temporal growth rates at increased Mach

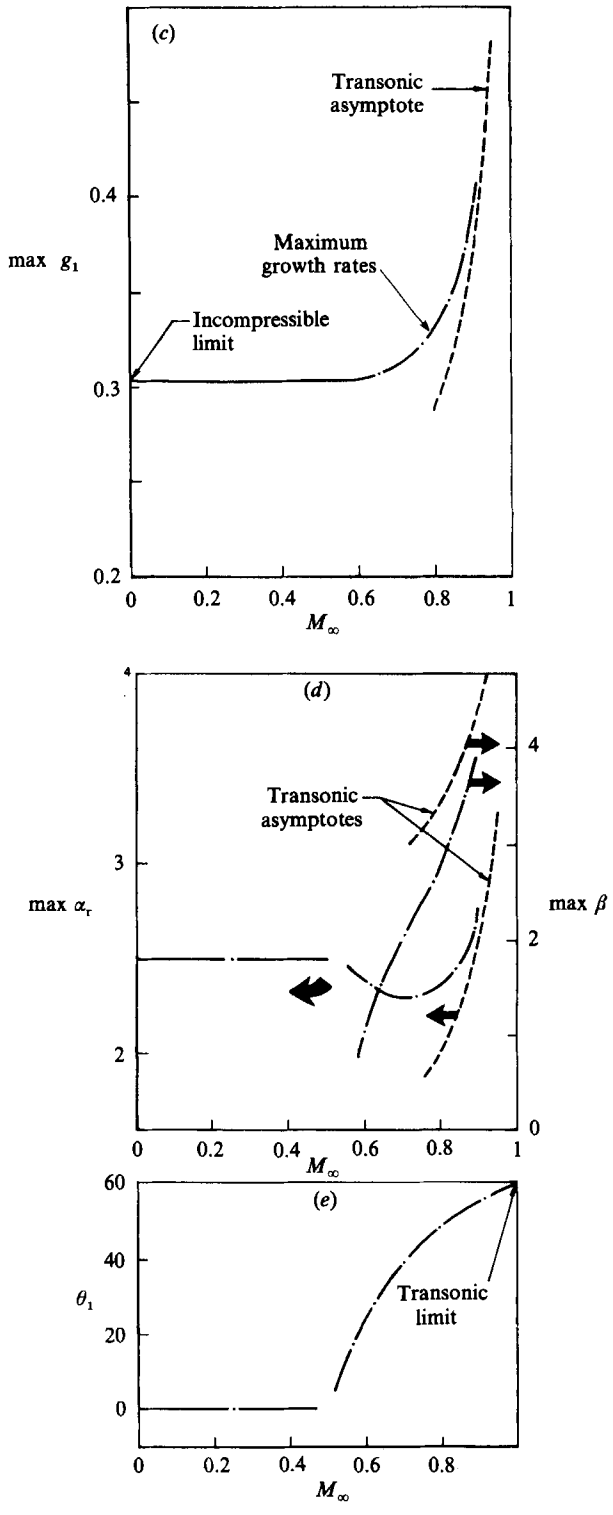

FIGURE 15. The normalized growth rates and other quantities in the subsonic regime (noted in §5), along with limits from the analogues of §4. (*a*) $M_\infty = 0$, (*b*) $M_\infty = 0.7$, (*c*) maximum growth rates, (*d*) wavenumbers, (*e*) wave angles.

numbers M_∞, according to the Orr–Sommerfeld results. The first modes are nevertheless of much interest physically and theoretically at all M_∞, in particular with regard to transition: see also below, and we note further Malik's (1987) suggestion that the first mode may dominate transition for an adiabatic wall at Mach numbers up to 7. An aspect of unknown significance, and perhaps only academic interest, found here is the double-mound formation in all the growth-rate curves for first modes, an aspect that is summarized at the end of §4. The first humps always give the maximum first-mode growth rate overall for a prescribed Mach number but, given that in practice the boundary-layer instability and transition (cf. further comments below) depend largely on the form of the input disturbances upstream, the second hump could sometimes play a major role, for example if the input disturbance contains mostly high wavenumbers. These second humps tend to become inviscid in the main, even though their growth rates are due to viscous forces, and there is a possible connection with Mack's inviscid second modes arising at higher Mach numbers.

The extremes of the Mach-number range are also intriguing and suggest some further developments, especially the hypersonic extreme where M_∞ becomes large. The lower, transonic, extreme for $M_\infty \to 1+$ leads into a new transonic regime which has been investigated by O. R. Burggraf and the present author (see also below), who find that there the link is established with subsonic stability properties as $M_\infty \to 1-$. The *subsonic* counterpart, which we have also studied here, has the term $\beta^2/(M_\infty^2-1)-\alpha^2$ in (2.12) replaced by $\alpha^2+\beta^2/(1-M_\infty^2)$. Its properties are summarized in figure 15: see also some earlier figures, and note that as the Mach number increases from zero the maximum normalized growth rate is for the two-dimensional first mode until the Mach number reaches approximately 0.5, after which the maximum switches to oblique waves. The subsonic version thereafter behaves much as in Case II of §4 as $M_\infty \to 1-$. Then, during the new *transonic* stage the three- and two-dimensional modes directed within the wave-Mach cones become elongated with increasing $M_\infty - 1$, eventually to emerge as non-parallel modes of $O(1)$ wavelength (and involving even larger scales, according to R. I. Bowles's subsequent research) in the supersonic regime as $M_\infty - 1$ rises to $O(1)$, in contrast with the three-dimensional modes whose directions lie outside the wave-Mach cones and which emerge to form the three-dimensional first modes of the supersonic regime studied in the present work. In the *hypersonic* extreme where $M_\infty \gg 1$ another new feature enters the reckoning, as follows. From Case I of §4 the principal range of the streamwise wavenumber concentrates into $\alpha \sim M_\infty^{-\frac{3}{2}}$ at large M_∞ (see (4.1)), so that the unscaled wavelength $L_x (\propto \alpha^{-1})$ involved then increases in the form

$$L_x \sim \{Re^{-\frac{3}{8}}(T_w^*/T_\infty^*)^{\frac{3}{2}} M_\infty^{-\frac{3}{4}}\} M_\infty^{\frac{3}{2}} \quad (M_\infty \gg 1) \tag{5.1}$$

in view of the scaling in (2.1). But under many conditions (see Stewartson 1964 and also below), including the insulated-wall example, the temperature ratio T_w^*/T_∞^* increases like M_∞^2 for the boundary layer at large M_∞ and so (5.1) implies that $L_x \sim Re^{-\frac{3}{8}} M_\infty^{\frac{15}{4}}$. Hence a new regime is encountered where

$$L_x \to O(1), \quad M_\infty \sim Re^{\frac{1}{10}}, \tag{5.2}$$

and the wavelength of the main first modes grows to become comparable with the $O(1)$ development length of the basic boundary layer, thus inducing substantial non-parallel-flow effects. In this new hypersonic regime, then, where the parameter

$$\bar{\kappa} \equiv M_\infty / Re^{\frac{1}{10}} \tag{5.3}$$

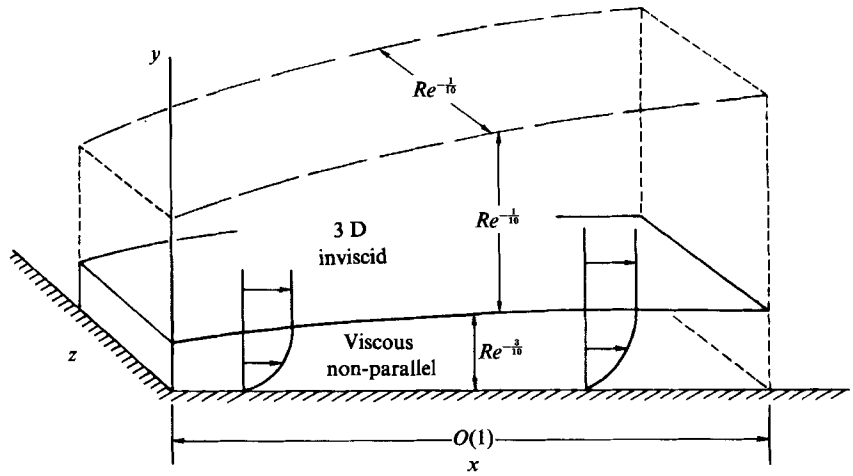

FIGURE 16. Sketch of the new hypersonic regime and its double structure when $M_\infty \sim Re^{\frac{1}{10}}$ (from §5), where non-parallel-flow effects become substantial.

is $O(1)$, the basic steady two-dimensional boundary layer simply has increased thickness $y \sim Re^{-\frac{3}{10}}$ (from (2.4a) with (5.3)) but the three-dimensional first modes of instability take on a novel structure as sketched in figure 16. This is because the lower deck, i.e. critical layer, expands in thickness like $Re^{-\frac{5}{8}}M_\infty^{-\frac{1}{4}}(T_w^*/T_\infty^*)^{\frac{3}{2}}\alpha^{-\frac{1}{3}}$ (from (2.2), (2.11a)), i.e. $Re^{-\frac{5}{8}}M_\infty^{\frac{13}{4}}$, to coalesce with the main deck of width $Re^{-\frac{1}{2}}(T_w^*/T_\infty^*)[\sim Re^{-\frac{1}{2}}M_\infty^2]$ exactly when $\bar{\kappa}$ reaches $O(1)$; meanwhile the upper deck contracts in width like $Re^{-\frac{3}{8}}M_\infty^{-\frac{7}{4}}(T_w^*/T_\infty^*)^{\frac{3}{2}}\alpha^{-1}$ $[\sim Re^{-\frac{3}{8}}M_\infty^{\frac{11}{4}}]$ for these dominant modes, from (2.5), (2.10a), to yield an outer width of $O(Re^{-\frac{1}{10}})$ in the stage $\bar{\kappa} \sim 1$. Hence the y-variation becomes two-tiered ($y \sim Re^{-\frac{3}{10}}$, $y \sim Re^{-\frac{1}{10}}$), the x-scale is $O(1)$, the z-scale contracts to $z \sim Re^{-\frac{1}{10}}$ (from (2.1), (4.1), (5.3)), the streamwise-pressure-gradient disturbance becomes negligible in the boundary layer, the timescale involved rises to $O(1)$ (from (2.1), (4.1), (5.3)), the maximum growth rate is for very oblique waves at nearly 90° to the free-stream direction, the viscous–inviscid interaction continues, but the waves are now crucially affected by non-parallelism. Other instability modes of interest such as the second-hump ones in (4.6) lead to other higher hypersonic regimes, as can excessively cooled or heated walls; we observe also that the regime (5.3) occurs at Mach numbers below the well-known hypersonic–viscous range $M_\infty \sim Re^{\frac{1}{8}}$ where the basic flow past the flat plate changes considerably (Stewartson 1964; Neiland 1970), introducing an outer shock layer, but the regime (5.3) for the main first modes seems the crucial one and it merits further study (N. D. Blackaby at UCL is currently conducting such a study).

Further investigation is also called for in the case of blunt-nosed bodies, for longitudinal vortices, with which the oblique Tollmien–Schlichting waves have a close connection, and for the impact of the restriction $M_\infty \ll Re^{\frac{1}{10}}$ (implied by (5.3)) on normal-mode decomposition, particularly regarding previous Orr–Sommerfeld computations. The above restriction reads

$$M_\infty \ll Re^{\frac{1}{10}} \quad \text{or} \quad M_\infty \ll R^{\frac{1}{5}}, \quad \text{or} \quad M_\infty \ll R_\delta^{\frac{1}{7}} \tag{5.4}$$

in terms of the local Reynolds numbers $R \equiv Re^{\frac{1}{2}}$ and R_δ based on the boundary-layer thickness, since $R_\delta \approx Re^{\frac{1}{2}}M_\infty^2$ in the hypersonic regime. Similar restrictions hold for other wall conditions. At a global Reynolds number Re of 2.25×10^6, say,

corresponding to $R = 1500$, the restriction (5.4) can be interpreted as meaning that the Orr–Sommerfeld approach holds only for $M_\infty \ll 4.3$, thus casting some doubt on the computations above about $M_\infty = 2$ shown in figures 5 and 9 and casting much doubt on the many Orr–Sommerfeld results presented at higher M_∞ values up to 10 and beyond. Such doubt obviously becomes even more severe at the lower Reynolds numbers R which are sometimes used in the computations, and it would seem to account for most of the differences in figures 5 and 9.

A move into the nonlinear disturbance properties in subsonic, supersonic and hypersonic boundary layers is also suggested by the present work, to shed more light on the compressible transition process. Here the problem posed in (2.3), (2.6) and the limiting cases described in the previous section provide the basis for computational and analytical studies of the effects of nonlinearity, including nonlinear interaction with longitudinal vortices, with the various first and second modes present and with cross-flow instabilities, some of which have already been addressed in recent work on the incompressible regime. We would draw attention here also to the nonlinear break-up phenomenon (within a finite time $\hat{t}$) which is applicable to (2.3), (2.6) among other interactive flows and is described by Smith (1988*a*), following Brotherton-Ratcliffe & Smith's (1987) and Smith's (1988*b*) studies of interactive nonlinear singularities.

Recent experiments concerning the first modes among other aspects are described by Maslov (1987, and private communication) and Lysenko & Maslov (1984) and these seem to be not inconsistent with the present theory. Somewhat related theoretical studies done or being done recently and independently are described by Duck (1987, and private communication) and Ryzhov (1987, and private communication).

The support of the United Technologies Independent Research Program is gratefully acknowledged, as are discussions with Drs M. J. Werle, J. E. Carter, J. M. Verdon, M. Y. Hussaini, M. Malik, Professor S. N. Brown, Mr N. D. Blackaby and Mr R. I. Bowles, and comments by the referees.

REFERENCES

Brotherton-Ratcliffe, R. V. & Smith, F. T. 1987 Complete breakdown of an unsteady interactive boundary layer (over a surface distortion or in a liquid layer). *Mathematika* **34**, 86–100.

Drazin, P. G. & Reid, W. H. 1981 *Hydrodynamic Stability*. Cambridge University Press.

Duck, P. W. 1987 Presentation at Euromech Colloquium, Exeter, UK.

Kendall, J. M. 1975 Wind-tunnel experiments relating to supersonic and hypersonic boundary-layer transition, *AIAA J.* **13**, 290–299.

Laufer, J. & Vrebalovich, T. 1960 Stability and transition of a laminar boundary layer on an insulated flat plate. *J. Fluid Mech.* **9**, 257–299.

Lysenko, V. I. & Maslov, A. A. 1984 The effect of cooling on supersonic boundary-layer stability. *J. Fluid Mech.* **147**, 39–52.

Mack, L. M. 1975 Linear stability theory and the problem of supersonic boundary-layer transition. *AIAA J.* **13**, 278–289.

Mack, L. M. 1984 Boundary-layer linear stability theory. *AGARD Rep.* 709.

Mack, L. M. 1986 In *Stability of Time Dependent and Spatially Varying Flows* (ed. D. L. Dwoyer & M. Y. Hussaini). Springer.

Malik, M. R. 1982 COSAL – a black-box compressible stability analysis code for transition prediction in three-dimensional boundary layers. *NASA CR*-165925.

MALIK, M. R. 1987 Prediction and control of transition in hypersonic boundary layers. *AIAA paper no.* 87-1414.

MASLOV, A. A. 1987 Presentation at Euromech Colloquium, Exeter, UK.

MILES, J. W. 1960 The hydrodynamic stability of a thin film of liquid in uniform shearing motion. *J. Fluid Mech.* **8**, 593–610.

NEILAND, V. YA. 1970 Upstream propagation of disturbances in hypersonic boundary layer interactions. *Izv. Akad. Nauk, SSSR, Mekh. Zhid.i Gaza*, **4**, 40–49.

PATE, S. R. & SCHUELER, C. J. 1969 Radiated aerodynamic noise effects on boundary-layer transition in supersonic and hypersonic wind tunnels. *AIAA J.* **7**, 450–457.

RYZHOV, O. S. 1987 Presentation at Euromech Colloquium, Exeter, UK.

SMITH, F. T. 1979*a* On the nonparallel flow stability of the Blasius boundary layer. *Proc. R. Soc. Lond.* A **366**, 91–109.

SMITH, F. T. 1979*b* Nonlinear stability of boundary layers for disturbances of various sizes. *Proc. R. Soc. Lond.* A **366**, 91–109; **368**, 573–589.

SMITH, F. T. 1985 Two-dimensional disturbance travel, growth and spreading in boundary layers. *UTRC* Rep. 85–36 (and see *J. Fluid Mech.* **169**, 1986, 353–377).

SMITH, F. T. 1986 The strong nonlinear growth of three-dimensional disturbances in boundary layers. *Utd. Tech. Res. Cent., E. Hartford, Conn., Rep.* UT 86-10.

SMITH, F. T. 1988*a* Finite-time break-up can occur in any unsteady interactive boundary layer. *Mathematika* (submitted).

SMITH, F. T. 1988*b* A reversed-flow singularity in interacting boundary layers. *Proc. R. Soc. Lond.* A (in press).

SMITH, F. T. & STEWART, P. A. 1987 The resonant-triad nonlinear interaction in boundary-layer transition. *J. Fluid Mech.* **179**, 227–252.

STEWARTSON, K. 1964 *Theory of Laminar Boundary Layers in Compressible Fluids.* Oxford University Press.

STEWARTSON, K. 1974 Multi-structured boundary layers on flat plates and related bodies. *Adv. Appl. Mech.* **14**, 145–239.

STEWARTSON, K. & WILLIAMS, P. G. 1969 Self-induced separation. *Proc. R. Soc. Lond.* A **312**, 181–206.